Research Article Vol. 12, No. 6 / 1 Jun 2022 / Optical Materials Express 2168
Optical Materials EXPRESS

Structure and mid-infrared optical properties of spin-coated polyethylene films developed for integrated photonics applications

Mauro David,[1] Davide Disnan,[2] Anna Lardschneider,[1] Dominik Wacht,[3] Hanh T. Hoang,[1] Georg Ramer,[3] Hermann Detz,[1,4] Bernhard Lendl,[3] Ulrich Schmid,[2] Gottfried Strasser,[1] and Borislav Hinkov[1,*]

[1]Institute of Solid State Electronics, TU Wien, Vienna, Austria
[2]Institute of Sensor and Actuator Systems, TU Wien, Vienna, Austria
[3]Institute of Chemical Technologies and Analytics, TU Wien, Vienna, Austria
[4]Central European Institute of Technology, Brno University of Technology, Brno, Czech Republic
*borislav.hinkov@tuwien.ac.at

Abstract: Polyethylene is a promising polymer for mid-infrared integrated optics due to its broad transparency and optimal refractive index. However, simple fabrication protocols that preserve its optical characteristics are needed to foster a wide range of applications and unlock its full potential. This work presents investigations of the optical and structural properties of spin-coated linear low-density polyethylene films fabricated under humidity-controlled conditions. The film thickness on polymer concentration dependence shows a non-linear behavior, in agreement with previously reported theoretical models and allowing predictive concentration-dependent thickness deposition with high repeatability. The surface roughness is on the nanometer-scale for all investigated concentrations between 1% and 10%. The crystallinity of the films was studied with the Raman spectroscopy technique. Mid-infrared ellipsometry measurements show a broad transparency range as expected for bulk material. Layer exposure to solvents revealed good stability of the films, indicating that the fabricated layers can outlast further fabrication steps. These investigations confirm the excellent properties of spin-coated thin films fabricated with our novel method, creating new opportunities for the use in photonic integrated circuits

1. Introduction

The mid-infrared (mid-IR) spectral range (~2–20 μm) is a part of the electromagnetic spectrum of particular scientific and technological interest for sensing applications and optical free-space communication. [1–3]. While laser sources operating at these wavelengths have developed into commercially available instruments over the last years, the advancement of integrated circuits has faced considerable challenges. A lot of work was dedicated to optimizing optoelectronic devices [4–7], including novel materials [8,9] and alternative architectures for mid-IR emission [10–12]. However, next-generation integration strategies [13,14], including implementation of novel transparent materials, were relatively scarce [15,16]. This is particularly true for the long-wave infrared (LWIR) spectral range, where an important atmospheric window is located (8–14 μm). There, the material selection of highly transparent materials with suitable characteristics and existing processing protocols is very limited [17,18]. This is particularly the case concerning the integration of these devices onto Indium Phosphide (InP) substrates for the realization of mid-IR photonic integrated circuits (PICs). Semiconductor- or Dielectric Loaded Surface Plasmon Polariton Waveguides (S/D-LSPPW) have been found to be a promising solution for these issues

#458667 https://doi.org/10.1364/OME.458667
Journal © 2022 Received 15 Mar 2022; revised 15 Apr 2022; accepted 21 Apr 2022; published 12 May 2022

Optical Materials EXPRESS

[14,15]. However, only a limited number of materials can simultaneously offer high transparency and low refractive index (to reduce interface reflections) to match their counterpart's performance at telecom frequencies (1.55 µm). Polymers have attracted tremendous interest for integrated optical applications for many years [19] but so far leaving out the LWIR spectral range. Their favorable optical characteristics, such as high transparency and low refractive index, are decisive factors for their use in optoelectronic devices and applications. PMMA and SU-8 are often used dielectric materials for plasmonic devices in the near-IR [20–22]. However, neither of both materials can offer high transparency in the mid-IR spectral range [23,24] due to numerous absorption lines especially located in the LWIR (see Fig. 1).

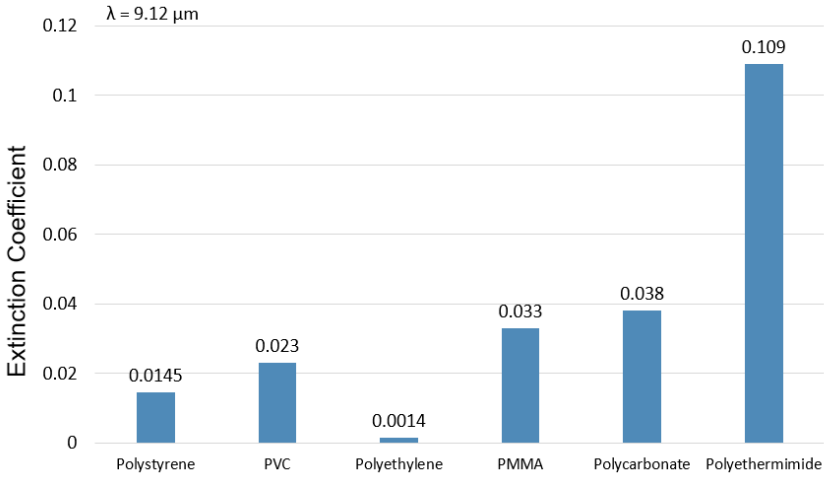

Fig. 1. Imaginary part of the complex refractive index at a wavelength of $\lambda = 9.12\,\mu m$ of some of the most transparent polymers in the LWIR. Data taken from [36,37]

In contrast, Polyethylene (PE) shows broad transparency for a wide spectral range [25]. It was so far exploited as broadband interconnector [26], flexible antenna [27], and sensor platform [28] in the THz spectral region (>20 µm). Theoretical investigations have shown its great potential as a core material for DLSPPW at telecom and THz frequencies [29] and as a cladding layer for hybrid plasmonic THz waveguides [30,31]. However, to unlock its full potential in the mid-IR with its much smaller geometrical dimensions, it is necessary to develop advantageous fabrication techniques that offer repeatable thin film deposition with excellent layer quality. The films are expected to have a composition similar to the bulk material, with low surface roughness and controlled thickness, while maintaining constant refractive index and high transparency. Moreover, suitable films must supply the necessary chemical and mechanical stability to outlast ambient exposure and further processing steps.

Several types of PE have been shown so far, and are typically classified according to their density and branching. The two basic types are High-Density PE (HDPE) and Low-Density PE (LDPE). HDPE is characterized by tightly packed molecules that form crystalline patches, while LDPE typically has a higher degree of amorphous fractions. In general, transparency tends to decrease with a higher degree of crystallization, as the light deflects along crystalline boundaries [32]. Therefore, the choice among the different PE types naturally falls towards LDPE, motivated by its higher transmittance compared to HDPE [33]. Nowadays, LDPE has almost entirely been replaced by linear LDPE (LLDPE), which has a higher melting temperature and crack strength [34,35].

Spin coating is a standard technique to produce high-quality and uniform polymer films of adjustable thickness on a plane substrate [38]. However, the state-of-the-art technology for

Optical Materials EXPRESS

producing spin-coated PE films is characterized by complex and time-consuming processes, including preheated equipment and employing toxic solvents (e.g., Decalin) used at their boiling temperatures, followed by several hours of annealing [39–41]. Furthermore, only very limited data already exists, reporting the mid-IR structural and optical properties of PE, and none in the case of layers produced by spin-coating [42]. Finally, addressing mid-IR applications, the thickness needs to be predicted precisely in the 100 nm – 6 µm range, which has not yet been realized in literature. In this context, we present an optimized fabrication technique performed by spin-coating of LLDPE with the scope of preserving its advantageous optical properties and obtaining high repeatable results in terms of layer thickness through controlling ambient conditions. The excellent optical properties of the films, and their stability towards solvent exposure, confirm that thin polyethylene layers obtained by our spin-coating technique can be used to realize the integration of crucial building elements for PIC devices.

2. Materials and methods

2.1. Materials

Double side polished 2-inch Si (100) wafers with 275 µm thickness were used as substrate material. They were cleaved into 11×11 mm^2 pieces, cleaned in an ultrasonic bath with acetone, rinsed in isopropanol, and dried with nitrogen. Subsequently, 8 nm of Ti and 100 nm of Au were sputtered (25 W, p_{work} = 8e-3 mbar) in multiple cycles (30 s per cycle), alternating with cool-down periods of 60 s, until reaching the desired film thickness.

LLDPE powder ($\rho = 0.906$ g/mL, average $M_w \sim 35000$ and $M_n \sim 7700$, used without further purification) was purchased from Sigma-Aldrich and dispersed in toluene (Sigma-Aldrich, anhydrous, purity 99.8%).

2.2. Polymer film fabrication

The fabrication of the films was conducted in a humidity-controlled glove box (see Fig. 2). A flow chart of the fabrication process is shown in Fig. 3.

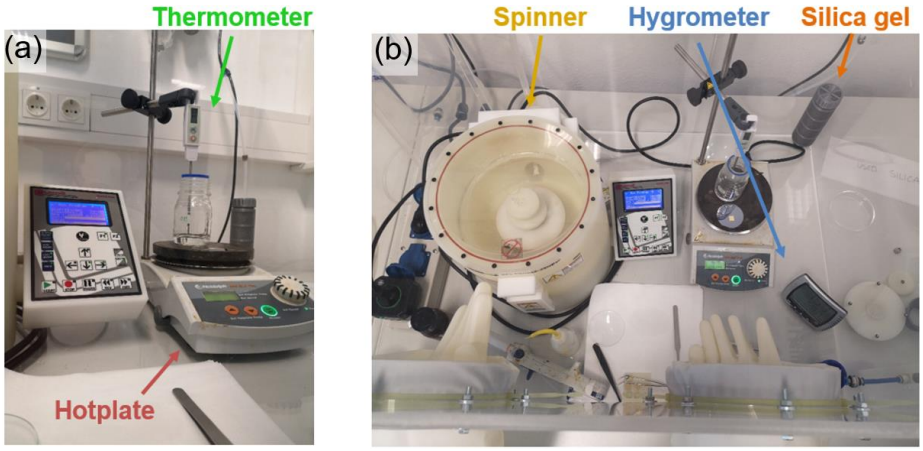

Fig. 2. Side (a) and top-view (b) pictures of the fabrication setup in the glove box. Temperature and humidity during fabrication were monitored with a digital hygrometer. The glove box stabilizes the humidity during the fabrication process by a constant supply of dry air flux and by the usage of silica gel grains. The relative humidity was kept at 15% ± 0.9% during the process.

Optical Materials EXPRESS

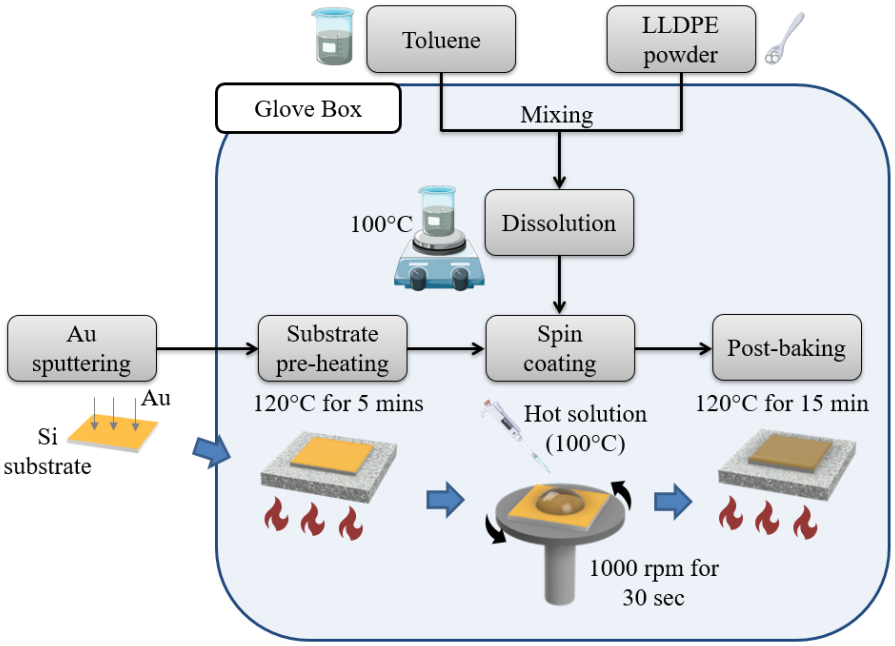

Fig. 3. Flow chart of the film fabrication process. The LLDPE powder was dissolved in toluene with different weight ratios, ranging from 1% to 10%, and stirred at 100 °C until complete dissolution. The temperature of the solution was tracked with a probe thermometer. Before depositing the polymer solution, the substrates were preheated on a hotplate set to 120 °C. The film was produced from the heated solution by using the dynamic dispense method (i.e., depositing the polymer solution on the substrate wafer during spinning) of a fixed amount of solution (100 µL). The spin-coating was carried out at 1000 rpm for 35 s with 5 seconds of acceleration for all coatings, followed by a post-baking at 120 °C for 15 min to evaporate any solvent residual.

2.3. Film characterization

The average thickness of the fabricated films was measured at three different spots on each sample with a Vis-Near-IR Ellipsometer (Woollam Alpha-SE, assuming $n_{LLDPE} \sim 1.54$ and measured n_{Au}). The measurements of the average film thickness of some of the thicker samples were also confirmed with a surface profilometer (Bruker Dektak XT, tip force 1 mg). The morphology analysis of the surface of the LLDPE layers was conducted with the profilometer first and then on the nanometer scale using Atomic Force Microscope (AFM). The measurements for the analysis with the surface profilometer were taken by scanning along the diagonal direction of the sample. Each scan was 8 mm long to ensure a complete overview of the surface inhomogeneities and roughness distribution in the inner part of the sample.

The standard practice for reliably extracting optical and electrical parameters of organic thin films is by spectrally resolved ellipsometry in the spectral range of interest [43]. Therefore, the optical properties of the fabricated layers were investigated using a mid-IR ellipsometer (IR-VASE, J.A Woollam) in the range of 2–12 µm.

After film fabrication, selected samples were submerged in deionized water and acetone for several minutes. This step was performed to confirm the robustness of the fabricated coatings to further processing steps with respect to adhesion and delamination of the films.

Film crystallinity was determined using Raman spectroscopy by fitting the CH_2 twisting band around 1300 cm^{-1}, as outlined by Lin et al. [44]. Raman spectra were collected using

Optical Materials EXPRESS

a confocal Raman spectrometer using a 532 nm laser source at 50 mW and a 100x (Zeiss EC Epiplan-Neofluar, NA 0.9) objective, using 10 s integration time and 10 averages. The spectrum was fit with two Gauss-Lorentz bands, one fixed at 1303 cm^{-1} and the second floating between 1290 cm^{-1} and 1295 cm^{-1}. The amorphous content was calculated as the ratio of the area of the 1303 cm^{-1} divided by the sum of both bands.

3. Results and discussion

3.1. Fabricated samples

Synthesis of PE-based thin films is typically performed at temperatures above 100 °C, with preheated equipment followed by long annealing times [45,41,39,46,40]. State-of-the-art techniques for spin coating LLDPE typically require the preheating of all the instrumentation (substrate, solution and spin coater chuck) to very high temperatures (>150 °C). Wang et al. [39] investigated the morphology of ultra-thin LLDPE films coated on HF passivated silicon wafers. To prevent the films from crystallizing, they dissolved polyethylene in boiling toluene and spun-cast the ht solution on heated substrates (150 °C). The films' thickness was controlled with the concentration (0.05–5%) and spin-coated with 2500 rpm, obtaining films with thickness between 10 and 460 nm. Two crystallization conditions have been studied to improve the surface quality: non-isothermal and isothermal. The first consisted of heating the fabricated films in an oil trapped vacuum oven at 140 °C for 30 min to melt the films. The temperature was then decreased to room temperature for 12 h before exposing the sample to the atmosphere. The isothermal process was performed by annealing to even higher temperatures for 30 min and then quickly moving to another vacuum oven set at 60 °C, where the samples were further annealed for 12 h before exposing them to room temperature. Under non-isothermal crystallization conditions, they obtained flat surfaces with typical spherulites. However, a discussion on the surface roughness of the fabricated films is missing. They reported a high difference of 10–15 nm between the lamellae ridges and the flat lamellae region and a degree of the amorphous fraction around 60%. Jeon and Krishnamoorti [40] investigated the individual effect of confinement and thermal history on the supermolecular and lamellae morphology variation by performing isothermal crystallization with different temperatures. For this purpose, they first dissolved LLDPE into boiling toluene and poured the solution into methanol at room temperature in order to precipitate the polymer after filtration, followed by overnight drying in a vacuum oven at 110 °C. Subsequently, the cleaned LLDPE sample was heated to 160 °C for 5 min and cooled at a rate of 100 °C for recrystallization and dissolved into boiling decalin (200 °C) for 1 h. The solution was then cooled and maintained at a temperature of 160 °C and spin coated at 1800 rpm with the static dispense method. To prevent early crystallization prior the spinning process, the spinner chuck was also preheated to 100–140 °C. They observed that the quality of the films strongly depended on the time of the acceleration period. At longer acceleration times the films were not macroscopically uniform. The concentration ranged from 0.15 to 3.5%, and they obtained thickness ranges between 20 to 800 nm. For isothermal crystallization studies, the spin-coated films were melted for 2 h at 160 °C in a vacuum oven, then quickly moved to a second preheated vacuum oven where they were isothermally crystallized over a temperature range of 90–119 °C for 2 h, and quickly quenched into liquid nitrogen. As the focus of the study was the morphological transitions upon crystallization procedure, data on the roughness and optical properties of the films are missing.

For many optoelectronic applications, roughness, transparency, and repeatability of a fabrication method are essential characteristics in order to obtain layers with desired thickness and sufficient (surface) quality. Ambient conditions may have a significant effect on spin-coated film properties. Typically, spin-coating processes of polymers are performed in research lab fume hoods, characterized by fluctuating relative humidity and temperature values, both also depending on ambient (weather) conditions. In contrast, glove boxes limit temperature and humidity fluctuations to a minimum. In general, the impact of the humidity on the film thickness is rather

Optical Materials EXPRESS

known [47,48], and it can create undesired thickness variation and lower layer quality. The variation in thickness ΔD of a spin-coated layer is related to the Relative Humidity (RH) through $\Delta D = (1\text{-}RH)^{\beta}$, where β is an empirically determined constant. Indeed, from some preliminary experiments performed in a standard lab fume hood, we obtained PE layers with a rather broad thickness range (between 200–500 nm for $wt = 2\%$). By performing the fabrication in the glove box, humidity fluctuations that affect the thickness repeatability are avoided.

As discussed previously, state-of-the-art processes involve dissolution at solvent boiling temperatures and preheated equipment. To avoid excess vaporization but ensure complete dissolution, we limited the temperature of the solution to 100 °C (i.e., ten degrees below the boiling point of the solvent). However, when using the static dispense method, we obtained inhomogeneous layers with low optical clarity, in agreement with the findings in literature [40]. We found that this issue is circumvented by using the dynamic dispense method. In this way, repeatable homogenous layers can be obtained. Films fabricated with this method show no visible inhomogeneities to the naked eye (Fig. 4). Moreover, after post-baking, the synthesized films were soaked in acetone and deionized water, proving strong adhesion to the underneath substrate. These are common steps performed in cleanrooms during photolithography-based processes for the fabrication of photonic devices, making the coatings' stability to these solvents essential for further developments. In contrast, the layers fabricated outside the glove box often experienced delamination and showed adhesion problems after the post-bake step.

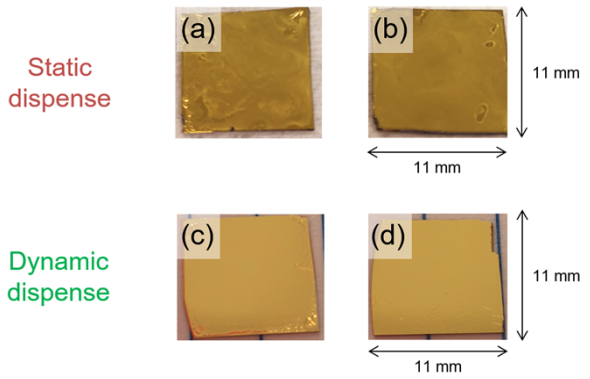

Fig. 4. Macroscopic pictures of fabricated samples in the glove box with deposition performed before spinning (a), (b), and during spinning (c),(d).

3.2. *Film thickness and concentration dependence*

From a device design perspective, it is desirable to be able to predict the thickness of the fabricated layers with relatively high precision from simple, measurable quantities. Typically, this is done by changing the concentration of the solution and/or the rotational speed of the spin coating process. In first approximation, the thickness depends more strongly on the concentration, and therefore we decided to fix the rotational speed to 1000 rpm (a rather low value as we aimed to relatively thick films). With our method, it was possible to repeatedly extract the non-linear film thickness dependence as a function of the LLDPE concentration from the films fabricated. To describe this behavior, we used the relation proposed by Chen [47] that models the thickness-dependence of a spin-coated layer from solvent type, solution, and spin coating parameters:

$$D = K_0 \mu^{0.36} \omega^{-0.50} \left(\frac{E\lambda}{C_\mu} \right)^{0.6} \tag{1}$$

Optical Materials EXPRESS

where D is the film thickness, K_0 is a constant for volatile organic solvents, μ is the viscosity of the coating solution, ω is the rotational speed, E is the solvent-evaporation rate, λ is the latent heat of evaporation and C_μ is the solvent heat capacity. Even though the relationship between viscosity and polymer concentration can be rather complex [45,49,50], it is possible to approximate it by a power-law function [45,51,52]. Therefore, the data were fitted to:

$$logD = C + 0.36\alpha(wt) \tag{2}$$

where C is a parameter that includes all the constants from Eq. (1), wt is the concentration, and α represents the coefficient describing the phenomenological power law that characterizes concentration and viscosity. In general, the viscous behavior of a solution can be estimated with good precision for higher concentrations, by expanding the viscosity-concentration equation into a Taylor series [50]:

$$\mu = \mu_0(1 + [\mu]wt + k_H[\mu]^2wt^2 + \cdots) \tag{3}$$

where $[\mu]$ is the intrinsic viscosity and k_H is the Huggins constant. Figure 5 shows the obtained results when fitting the thickness to the model. From our measurements, we could extract two distinct values of α that divide the solution into two regimes. We obtained a value of $\alpha = 2.8$ for concentrations ranging between 1 and 4%, indicating that the solution in this concentration range can be considered viscoelastic [52]. For concentrations above 5% we extracted a value of $\alpha = 7.72$. This relatively high value indicates that the solution is in a *highly concentrated* regime, typically characterized by entangled macromolecules [49,50,52].

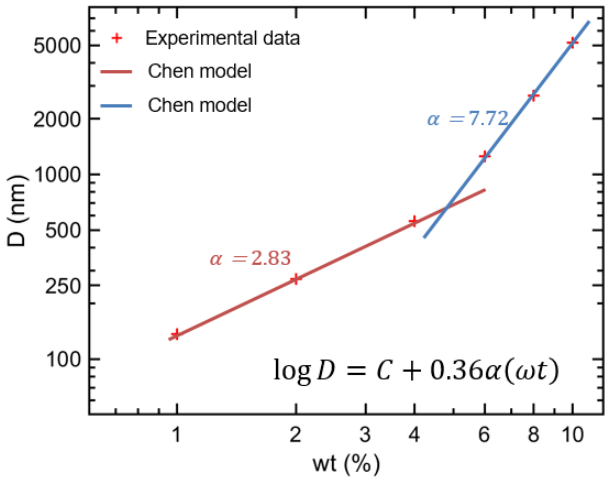

(a)

wt (%)	D (nm)	α
1	138 ± 1	2.83
2	271 ± 4	2.83
4	560 ± 11	2.83
6	1246 ± 13	7.72
8	2670 ± 2	7.72
10	5186 ± 17	7.72

(b)

Fig. 5. (a) Film thickness dependence on LLDPE concentration including experimental datapoints (red crosses) and fits of the model in both obtained regimes (solid line). All films were fabricated in the glove box. (b) Table reporting the precise thickness values measured with the ellipsometer.

To test the repeatability of our fabrication method, we fabricated 10 coatings with mass portion of 10%. The average measured thickness was 5159 ± 87 nm, showing the excellent repeatability of our fabrication process.

3.3. Morphology analysis of films

LLDPE typically presents a degree of crystallinity ranging from 20% to 50% [32,39,44] and, therefore, naturally tends to arrange into a more amorphous phase. Since the scope of our work is

Optical Materials EXPRESS

to attain homogenous and transparent coatings, we did not need to focus on achieving a maximal degree of crystallization, because it would have been counterproductive, as described in the introduction.

AFM surface scans of the fabricated LLDPE films of different polymer concentrations are presented in Fig. 6. Different arrangements of chains along the surface can be identified from the height profile recorded with the AFM. The bright areas are connected to a higher polymer chains concentration. However, since we did not perform any isothermal or non-isothermal crystallization process, no highly structured and ordered morphology based on spherulites can be observed. From Fig. 6, it can be seen that increasing the percentage of LLDPE dissolved in the solution results in an enlargement of the polymer microstructure. The surface features of the LLDPE thin films become more prominent as the polymer concentration increases, without affecting the general characteristics of the chain arrangement. Furthermore, the surface's height recorded by the AFM increases by the enlargement of the microstructure.

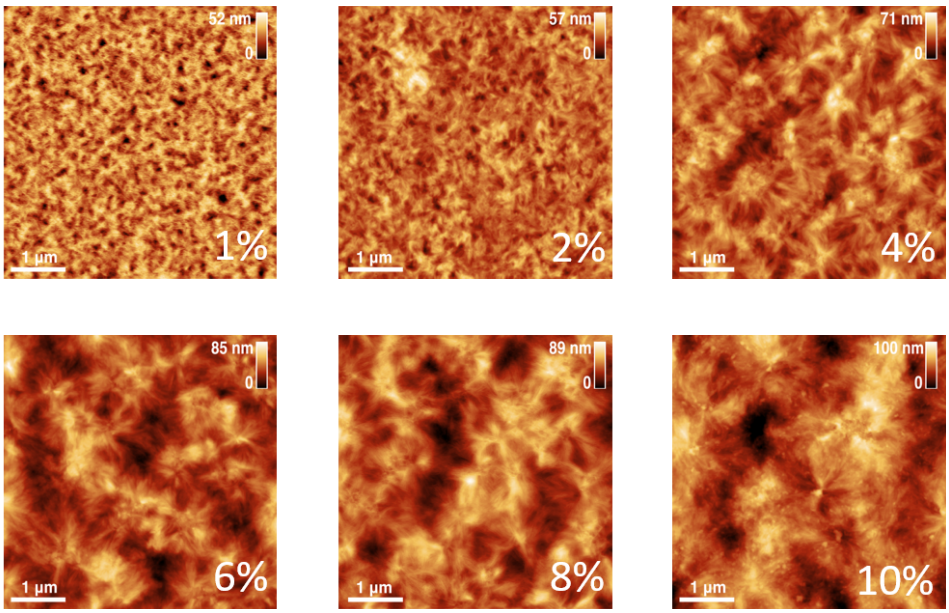

Fig. 6. AFM images of LLDPE thin film surfaces for different mass concentrations. The change in ordering of the structures in the different regimes can be observed.

In order to evaluate the quality of the layers, we determined the mean roughness as a function of the polymer concentration from the AFM measurements (Fig. 7). Even though the surface roughness increases with concentration, it remains below 15 nm for all concentrations.

The surface of the films, analyzed by the profilometer, does not reveal inhomogeneities on the mm-scale across the samples. Such "wavy-like" fluctuations of the thickness have been observed in previous studies on PE coatings [39] and are associated with the Gibbs-Marangoni effect.

3.4. Film crystallinity

The amorphous content of the film was found to decrease with increasing LLDPE concentration in the coating solution (see Fig. 8) from around 80%(m/m) at 1% concentration down to around 65%(m/m) at 10% (fitted spectrum is provided in Supplement 1). Similarly, the variance of amorphous content was found to decrease with increasing PE content. However, as Raman spectra represent the make up of an area smaller than 500 nm in diameter, the decrease in standard deviation can be interpreted as being in part dependent on the homogeneity of the film. A higher

Optical Materials EXPRESS

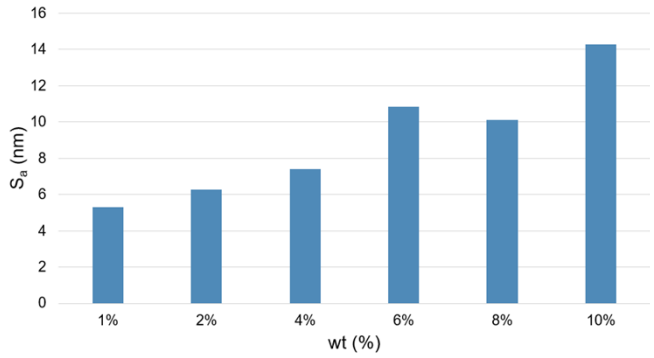

Fig. 7. Mean roughness (S_a) versus concentration for the different concentrations of LLDPE.

concentration of the stock solution leads not only to a decrease in amorphous fraction of the film, but also to more homogeneous films.

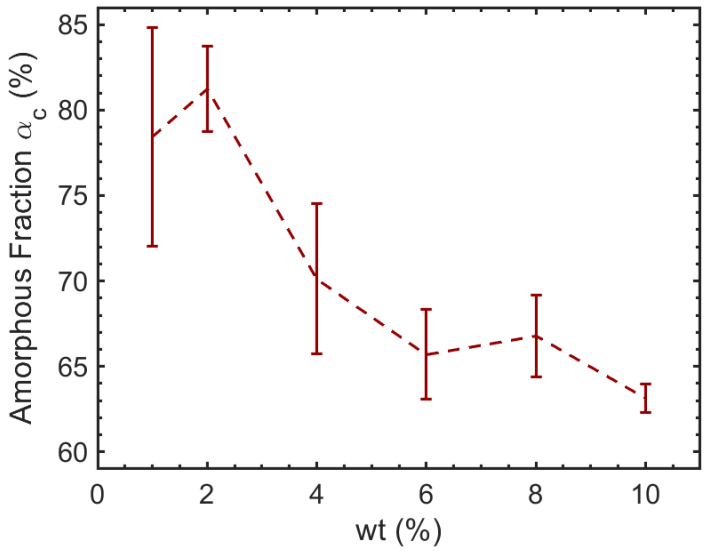

Fig. 8. Mass fraction of amorphous content of the film, as determined from confocal Raman spectroscopy. Error bars represent the standard deviation of measurements taken in 5 different locations.

3.5. Mid-infrared optical characterization

The wavelength-dependent mid-IR refractive index and permittivity profile of a typical LLDPE film fabricated in the glove box is shown in Fig. 9 (the table with the data is provided in Supplement 1). We thus expected their presence due to the intrinsic polymer interband transitions [3]. The high transparency of the fabricated films is experimentally confirmed, indicating the excellent optical properties of the fabricated layers at mid-IR to LWIR frequencies.

This data presents the first mid-IR ellipsometry measurement of spin-coated LLDPE and confirms the potential of our fabrication technique for producing robust, controllable, and time-efficient LLDPE coatings. Due to the optimal refractive index characteristics, they can be employed as passivation layers, antireflection-coating, and waveguides (cladding or core)

Optical Materials EXPRESS

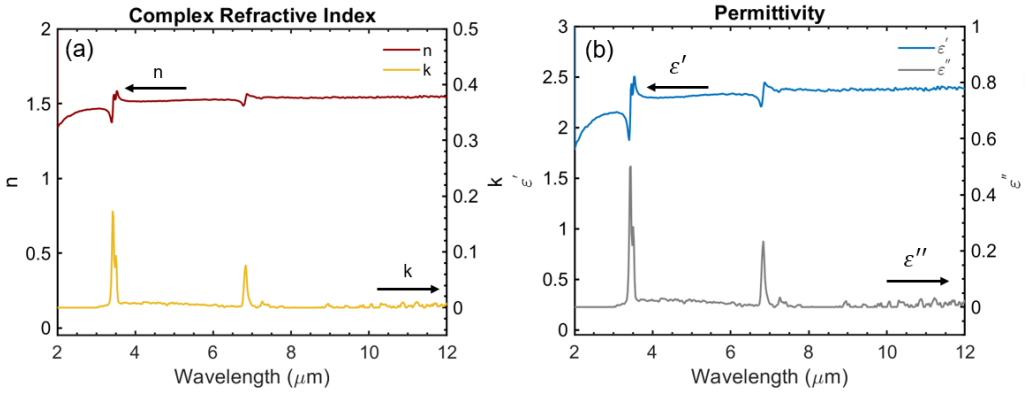

Fig. 9. (a) Refractive index and (b) complex permittivity of LLDPE thin films (thickness = 270 nm, *wt* = 2%). The three most characteristic hydrocarbon peaks of PE are located around 3.4, 3.5, and 6.8 μm (2923, 2849, and 1473 cm^{-1}).

material for new mid-IR and especially LWIR integrated optoelectronics. For many polymers, photodegradation due to UV exposure can be an issue for outdoor applications. However, for integrated optics applications, the possibility of having UV-sensitive polymers can be an advantage. Photolithography-based processes can be used in order to create spatial changes for circuit patterning. As an example, photolithography-based fabrication of polyethylene terephthalate substrates shaped into optical waveguides was recently exploited for sensing applications at telecom frequencies [53], where a channel waveguide is formed by etching pores in the cladding region by a NaOH solution at 60 °C after UV exposure to degrading the polymer. A similar technique can be used to pattern spin-coated PE films deposited on different chips. As discussed in the introduction, for near-IR DLSPPW, PMMA is often the polymer selected as optical waveguide core [54]. However, since another photosensitive resin needs to be applied (photo-resist) in order to obtain circuit patterning, the core is typically protected through an inorganic barrier before dry etching the polymer layer. A similar process can also be used to pattern a PE film in order to obtain the desired optical circuit.

Therefore, based on our fabrication method, we create new opportunities to integrate this material into various mid-IR optoelectronic applications, particularly for sensing and the next generation of LWIR free-space optical communication. Moreover, due to the material's extraordinary chemical and mechanical properties, more applications can be exploited, for example, the fabrication of microfluidic chips in combination with new monolithic sensor concepts in this spectral range [14].

4. Conclusions

We report a novel and optimized fabrication technique to obtain smooth, high-quality LLDPE films on Au layers. The optimization of the process was obtained by producing the films under humidity-controlled conditions. The presented technique avoids using more complex and time-consuming processes with a preheated chuck and allows easy control of the film thickness by changing LLDPE concentration. Indeed, it was possible to derive the non-linear power of low thickness dependency versus concentration, in agreement with previously reported theoretical models. The thicknesses obtained ranged from 138 nm to 5.2 μm, depending on polymer concentration, with excellent repeatability and low roughness (<15 nm). Furthermore, the layers have high stability when subjected to solvent exposure, indicating the potential robustness to further processing steps. The crystallinity was studied with the Raman spectroscopy

Optical Materials EXPRESS

technique, revealing an amorphous content between 60–80%. The fabricated films display broad transparency through the whole mid-IR spectral range, with an almost constant refractive index (n~1.5) throughout the whole range, as expected for the bulk material. Overall, the simplicity of our fabrication approach, combined with excellent optical properties, makes LLDPE films highly suitable candidates for polymer-based mid-IR optoelectronic applications such as coatings, passivation layers, and waveguides.

Funding. Horizon 2020 Framework Programme (828893); Austrian Science Fund (M2485-N34).

Acknowledgments. We acknowledge the CzechNanoLab Research Infrastructure supported by MEYS CR (LM2018110) for the expert technical assistance. The authors want to acknowledge funding through the Horizon 2020 Framework Programme (project cFlow, 828893). Fruitful discussions with Werner Schrenk, Aaron Maxwell Andrews, Masiar Sistani and Catarina Santos are gratefully acknowledged.

Disclosures. The authors declare no conflicts of interest related to this article

Data availability. Data underlying the results presented in this paper are not publicly available at this time but may be obtained from the authors upon reasonable request.

Supplemental document. See Supplement 1 for supporting content.

References

1. "Extending opportunities," Nature Photon **6**(7), 407 (2012).
2. J. Hu, J. Meyer, K. Richardson, and L. Shah, "Feature issue introduction: mid-IR photonic materials," Opt. Mater. Express **3**(9), 1571–1575 (2013).
3. M. Sieger and B. Mizaikoff, "Toward on-chip mid-infrared sensors," Anal. Chem. **88**(11), 5562–5573 (2016).
4. B. Schwarz, C. A. Wang, L. Missaggia, T. S. Mansuripur, P. Chevalier, M. K. Connors, D. McNulty, J. Cederberg, G. Strasser, and F. Capasso, "Watt-level continuous-wave emission from a bifunctional quantum cascade laser/detector," ACS Photonics **4**(5), 1225–1231 (2017).
5. A. Jollivet, B. Hinkov, S. Pirotta, H. Hoang, S. Derelle, J. Jaeck, M. Tchernycheva, R. Colombelli, A. Bousseksou, M. Hugues, N. Le Biavan, J. Tamayo-Arriola, M. Montes Bajo, L. Rigutti, A. Hierro, G. Strasser, J.-M. Chauveau, and F. H. Julien, "Short infrared wavelength quantum cascade detectors based on m-plane ZnO/ZnMgO quantum wells," Appl. Phys. Lett. **113**(25), 251104 (2018).
6. B. Hinkov, A. Bismuto, Y. Bonetti, M. Beck, S. Blaser, and J. Faist, "Singlemode quantum cascade lasers with power dissipation below 1 W," Electron. Lett. **48**(11), 646 (2012).
7. Y. Bai, N. Bandyopadhyay, S. Tsao, S. Slivken, and M. Razeghi, "Room temperature quantum cascade lasers with 27% wall plug efficiency," Appl. Phys. Lett. **98**(18), 181102 (2011).
8. B. Hinkov, H. T. Hoang, M. Hugues, J.-M. Chauveau, and G. Strasser, "Etching of m-plane Zn(Mg)O epitaxial films and its impact on surface leakage currents," Semicond. Sci. Technol. **36**(3), 035023 (2021).
9. H. Machhadani, P. Kandaswamy, S. Sakr, A. Vardi, A. Wirtmüller, L. Nevou, F. Guillot, G. Pozzovivo, M. Tchernycheva, A. Lupu, L. Vivien, P. Crozat, E. Warde, C. Bougerol, S. Schacham, G. Strasser, G. Bahir, E. Monroy, and F. H. Julien, "GaN/AlGaN intersubband optoelectronic devices," New J. Phys. **11**(12), 125023 (2009).
10. H. Knötig, B. Hinkov, R. Weih, S. Höfling, J. Koeth, and G. Strasser, "Continuous-wave operation of vertically emitting ring interband cascade lasers at room temperature," Appl. Phys. Lett. **116**(13), 131101 (2020).
11. B. Hinkov, M. Beck, E. Gini, and J. Faist, "Quantum cascade laser in a master oscillator power amplifier configuration with Watt-level optical output power," Opt. Express **21**(16), 19180–19186 (2013).
12. M. J. Suess, P. Jouy, C. Bonzon, J. M. Wolf, E. Gini, M. Beck, and J. Faist, "Single-mode quantum cascade laser array emitting from a single facet," IEEE Photonics Technol. Lett. **28**(11), 1197–1200 (2016).
13. L. Diehl, B. G. Lee, P. Behroozi, M. Loncar, M. Belkin, F. Capasso, T. Aellen, D. Hofstetter, M. Beck, and J. Faist, "Microfluidic tuning of distributed feedback quantum cascade lasers," Opt. Express **14**(24), 11660 (2006).
14. B. Schwarz, P. Reininger, D. Ristanić, H. Detz, A. M. Andrews, W. Schrenk, and G. Strasser, "Monolithically integrated mid-infrared lab-on-a-chip using plasmonics and quantum cascade structures," Nat. Commun. **5**(1), 4085 (2014).
15. M. David, A. Dabrowska, M. Sistani, I. C. Doganlar, E. Hinkelmann, H. Detz, W. M. Weber, B. Lendl, G. Strasser, and B. Hinkov, "Octave-spanning low-loss mid-IR waveguides based on semiconductor-loaded plasmonics," Opt. Express **29**(26), 43567 (2021).
16. R. Wang, P. Täschler, Z. Wang, E. Gini, M. Beck, and J. Faist, "Monolithic integration of mid-infrared quantum cascade lasers and frequency combs with passive waveguides," ACS Photonics **9**(2), 426–431 (2022).
17. H. Lin, Z. Luo, T. Gu, L. C. Kimerling, K. Wada, A. Agarwal, and J. Hu, "Mid-infrared integrated photonics on silicon: a perspective," Nanophotonics **7**(2), 393–420 (2017).
18. A. Osman, M. Nedeljkovic, J. S. Penades, Y. Wu, Z. Qu, A. Z. Khokhar, K. Debnath, and G. Z. Mashanovich, "Suspended low-loss germanium waveguides for the longwave infrared," Opt. Lett. **43**(24), 5997–6000 (2018).

Optical Materials EXPRESS

19. X.-Y. Han, Z.-L. Wu, S.-C. Yang, F.-F. Shen, Y.-X. Liang, L.-H. Wang, J.-Y. Wang, J. Ren, L.-Y. Jia, H. Zhang, S.-H. Bo, G. Morthier, and M.-S. Zhao, "Recent progress of imprinted polymer photonic waveguide devices and applications," Polymers **10**(6), 603 (2018).
20. M. A. Sefunc, M. Pollnau, and S. M. García-Blanco, "Low-loss sharp bends in polymer waveguides enabled by the introduction of a thin metal layer," Opt. Express **21**(24), 29808–29817 (2013).
21. A. Block, C. Etrich, T. Limboeck, F. Bleckmann, E. Soergel, C. Rockstuhl, and S. Linden, "Bloch oscillations in plasmonic waveguide arrays," Nat. Commun. **5**(1), 3843 (2014).
22. T. J. Davis, D. E. Gómez, and A. Roberts, "Plasmonic circuits for manipulating optical information," Nanophotonics **6**(3), 543–559 (2016).
23. S. Tsuda, S. Yamaguchi, Y. Kanamori, and H. Yugami, "Spectral and angular shaping of infrared radiation in a polymer resonator with molecular vibrational modes," Opt. Express **26**(6), 6899–6915 (2018).
24. E. Motaharifar, R. G. Pierce, R. Islam, R. Henderson, J. W. P. Hsu, and M. Lee, "Broadband Terahertz Refraction Index Dispersion and Loss of Polymeric Dielectric Substrate and Packaging Materials," J Infrared Milli Terahz Waves **39**(1), 93–104 (2018).
25. D. R. Smith and E. V. Loewenstein, "Optical constants of far infrared materials 3: plastics," Appl. Opt. **14**(6), 1335 (1975).
26. H. I. Song, H. Jin, and H.-M. Bae, "Plastic straw: future of high-speed signaling," Sci Rep **5**(1), 16062 (2015).
27. M. Geiger, M. Hitzler, J. Iberle, and C. Waldschmidt, "A dielectric lens antenna fed by a flexible dielectric waveguide at 160 GHz," in *2017 11th European Conference on Antennas and Propagation (EUCAP)* (2017), pp. 3380–3383.
28. B. You, J.-Y. Lu, T.-A. Liu, and J.-L. Peng, "Hybrid terahertz plasmonic waveguide for sensing applications," Opt. Express **21**(18), 21087–21096 (2013).
29. X. Y. He, Q. J. Wang, and S. F. Yu, "Analysis of dielectric loaded surface plasmon waveguide structures: Transfer matrix method for plasmonic devices," J. Appl. Phys. **111**(7), 073108 (2012).
30. B. Zhang, Y. Bian, L. Ren, F. Guo, S.-Y. Tang, Z. Mao, X. Liu, J. Sun, J. Gong, X. Guo, and T. J. Huang, "Hybrid dielectric-loaded nanoridge plasmonic waveguide for low-loss light transmission at the subwavelength scale," Sci. Rep. **7**(1), 40479 (2017).
31. B. You, J.-Y. Lu, W.-L. Chang, C.-P. Yu, T.-A. Liu, and J.-L. Peng, "Subwavelength confined terahertz waves on planar waveguides using metallic gratings," Opt. Express **21**(5), 6009–6019 (2013).
32. A. Peacock, *Handbook of Polyethylene: Structures: Properties, and Applications* (CRC Press, 2000).
33. A. Martínez-Romo, R. González-Mota, J. J. Soto-Bernal, and I. Rosales-Candelas, "Investigating the degradability of HDPE, LDPE, PE-BIO, and PE-OXO films under UV-B radiation," Journal of Spectroscopy **2015**, 1–6 (2015).
34. C. Vasile and M. Pascu, *Practical Guide to Polyethylene* (iSmithers Rapra Publishing, 2005).
35. P. N. Khanam and M. A. A. AlMaadeed, "Processing and characterization of polyethylene-based composites," Advanced Manufacturing: Polymer & Composites Science **1**(2), 63–79 (2015).
36. T. L. Myers, R. G. Tonkyn, T. O. Danby, M. S. Taubman, B. E. Bernacki, J. C. Birnbaum, S. W. Sharpe, and T. J. Johnson, "Accurate measurement of the optical constants n and k for a series of 57 inorganic and organic liquids for optical modeling and detection," Appl Spectrosc **72**(4), 535–550 (2018).
37. X. Zhang, "Complex refractive indices measurements of polymers in infrared bands," Journal of Quantitative Spectroscopy and Radiative Transfer **252**, 107063 (2020).
38. R. Das and A. Chanda, "Fabrication and properties of spin-coated polymer films," *Nano-size Polymers* (Springer, 2016), pp. 283–306.
39. Y. Wang, S. Ge, M. Rafailovich, J. Sokolov, Y. Zou, H. Ade, J. Lüning, A. Lustiger, and G. Maron, "Crystallization in the thin and ultrathin films of poly(ethylene−vinyl acetate) and linear low-density polyethylene," Macromolecules **37**(9), 3319–3327 (2004).
40. K. Jeon and R. Krishnamoorti, "Morphological behavior of thin linear low-density polyethylene films," Macromolecules **41**(19), 7131–7140 (2008).
41. O. Mellbring, S. Kihlman Øiseth, A. Krozer, J. Lausmaa, and T. Hjertberg, "Spin coating and characterization of thin high-density polyethylene films," Macromolecules **34**(21), 7496–7503 (2001).
42. Y. Wang, Y. Abe, Y. Matsuura, M. Miyagi, and H. Uyama, "Refractive indices and extinction coefficients of polymers for the mid-infrared region," Appl. Opt. **37**(30), 7091 (1998).
43. N. Nosidlak, P. Dulian, D. Mierzwiński, and J. Jaglarz, "The determination of the electronic parameters of thin amorphous organic films by ellipsometric and spectrophotometric study," Coatings **10**(10), 980 (2020).
44. W. Lin, M. Cossar, V. Dang, and J. Teh, "The application of Raman spectroscopy to three-phase characterization of polyethylene crystallinity," Polym. Test. **26**(6), 814–821 (2007).
45. K. A. Dill, "Concentration dependence of the viscosity and viscoelasticity of polymer solutions: application of the theory of Muthukumar and Freed," Macromolecules **13**(3), 620–622 (1980).
46. A. C. Wirtz, M. Dokter, C. Hofmann, and E. J. J. Groenen, "Spincoated polyethylene films for single-molecule optics," Chem. Phys. Lett. **417**(4-6), 383–388 (2006).
47. B. T. Chen, "Investigation of the solvent-evaporation effect on spin coating of thin films," Polym. Eng. Sci. **23**(7), 399–403 (1983).
48. P. N. Plassmeyer, G. Mitchson, K. N. Woods, D. C. Johnson, and C. J. Page, "Impact of relative humidity during spin-deposition of metal oxide thin films from aqueous solution precursors," Chem. Mater. **29**(7), 2921–2926 (2017).

Optical Materials EXPRESS

49. N. Chapman, M. Chapman, and W. B. Euler, "Modeling of poly(methylmethacrylate) viscous thin films by spin-coating," Coatings **11**(2), 198 (2021).
50. S. Matsuoka and M. K. Cowman, "Equation of state for polymer solution," Polymer **43**(12), 3447–3453 (2002).
51. E. Hedl, I. Fabijanić, I. Šrut Rakić, I. Vadla, and J. Sancho-Parramon, "Fabrication by spin-coating and optical characterization of poly(styrene-co-acrylonitrile) thin films," Coatings **11**(9), 1015 (2021).
52. A. Weill and E. Dechenaux, "The spin-coating process mechanism related to polymer solution properties," Polym. Eng. Sci. **28**(15), 945–948 (1988).
53. W. F. Ho, H. Chan, and V. Tsvetkov, "Porous polyethylene terephthalate optical waveguide for sensing applications," IEEE Photonics Technology Letters **25**, 1672 (2013).
54. A. Kumar, J. Gosciniak, V. S. Volkov, S. Papaioannou, D. Kalavrouziotis, K. Vyrsokinos, J.-C. Weeber, K. Hassan, L. Markey, A. Dereux, T. Tekin, M. Waldow, D. Apostolopoulos, H. Avramopoulos, N. Pleros, and S. I. Bozhevolnyi, "Dielectric-loaded plasmonic waveguide components: Going practical," Laser & Photonics Reviews **7**(6), 938–951 (2013).